Superconductivity in $BaIrSi_2$: A 5*d* electron system with a noncentrosymmetric crystal structure

Masaaki Isobe,[1,*] Koji Kimoto,[2] Masao Arai,[3] and Eiji Takayama-Muromachi[4]

[1]*Research Center for Functional Materials, National Institute for Materials Science, 1-1 Namiki, Tsukuba, Ibaraki 305-0044, Japan*

[2]*Research Center for Advanced Measurement and Characterization, National Institute for Materials Science, 1-1 Namiki, Tsukuba, Ibaraki 305-0044, Japan*

[3]*International Center for Materials Nanoarchitectonics, National Institute for Materials Science, 1-1 Namiki, Tsukuba, Ibaraki 305-0044, Japan*

[4]*National Institute for Materials Science, 1-2-1 Sengen, Tsukuba, Ibaraki 305-0047, Japan*

(Received 13 October 2018; revised manuscript received 3 December 2018; published 22 February 2019)

The compound $BaIrSi_2$ was successfully synthesized under high pressure at 6 GPa. $BaIrSi_2$ crystalizes in an orthorhombic symmetry with the noncentrosymmetric space group $C222_1$ and the lattice parameters $a = 15.0492(1)$ Å, $b = 8.0311(1)$ Å, and $c = 8.0314(1)$ Å. $BaIrSi_2$ shows superconductivity below a critical temperature $T_c \sim 6$ K and an upper critical field $\mu_0 H_{c2}(0) \sim 6$ T with a Ginzburg-Landau parameter $\kappa_{GL} \sim 87$. Specific-heat measurements suggest that $BaIrSi_2$ is an intermediate-coupling superconductor with a moderate electron-phonon coupling constant $\lambda_{ep} \sim 0.8$. The Sommerfeld constant is $\gamma_n \sim 5.5\,\mathrm{mJ/mole\,K^2}$. Phonon mediation seems to be dominant for Cooper pairing in $BaIrSi_2$. The *ab initio* calculations revealed that $BaIrSi_2$ has four Fermi surfaces split by spin-orbit coupling. The Cooper pairing seems to occur between electrons without spin degeneracy.

DOI: 10.1103/PhysRevB.99.054514

I. INTRODUCTION

Recently, there has been an increasing interest in 5*d* electron systems such as iridium compounds, because of their strong spin-orbit coupling (SOC), which can lead to fascinating and unusual electronic states cooperating with electronic correlation and symmetry [1–3]. In particular, the superconductivity affected by SOC in noncentrosymmetric systems has attracted much attention from many solid-state physicists and chemists [4–11]. The term "noncentrosymmetric" means the crystallographic symmetry of a lattice has no inversion center in the crystal structure. In such compounds, the asymmetric atomic positioning induces a local anisotropic crystal field, lifting the twofold spin degeneracy of the electronic band through SOC, and may split a Fermi surface into two. If such an electron system is transferred into a superconducting state at low temperature, under the condition that the energy difference between the split bands is larger than the superconducting-gap energy scale, Cooper pairs can be formed by the electrons without spin degeneracy as an inherent feature. This is the so-called parity mixing state, in which spin singlets and spin triplets coexist for the spin component in the wave function [4–11]. In this case, that is to say, in "noncentrosymmetric superconductivity," the parity mixing state is expected to cause a two-component superconducting-gap order parameter, and line nodes may appear on the inner Fermi surface, yielding an anisotropic superconductivity regardless of the origin of the pairing attractive force between electrons.

So far, a great number of noncentrosymmetric superconductors have been reported. Among them, heavy-fermion *f* electron systems such as $CePt_3Si$ [12], $CeRhSi_3$ [13], $CeIrSi_3$ [14], $CeCoGe_3$ [15], and UIr [16] triggered research on noncentrosymmetric superconductivity. Some of the compounds exhibit an incredibly high upper critical field H_{c2}, far superior to the Pauli limit expected from the BCS theory. The unusually high H_{c2} is attributed to the antisymmetric SOC in the noncentrosymmetric structure. It is believed that electronic correlation can enhance the characteristic features of noncentrosymmetric superconductivity. However, in the *f* electron system its critical temperature T_c is considerably low, typically around 1 K, and in many cases pressurization is necessary for inducing superconductivity. Pressurization is an obstacle to precise measurements of physical properties. It is therefore desirable to obtain higher-T_c noncentrosymmetric superconductors with high H_{c2} under ambient pressure. From this point of view, it is also worth expanding the research to noncentrosymmetric superconductors without *f* electrons. Thus far, many *f*-electron-free noncentrosymmetric superconductors have been reported, e.g., $BaPtSi_3$ [17], $CaIrSi_3$ [18], $CaPtSi_3$ [18], $SrAuSi_3$ [19], Li_2Pd_3B [20], Li_2Pt_3B [21], Ru_7B_3 [22], $Mg_{10}Ir_{19}B_{16}$ [23], Mo_3Al_2C [24], $LaNiC_2$ [25], Y_2C_3 [26,27], La_2C_3 [28], BiPd [29], Re_3W [30], Rh_2Ga_9 [31], Ir_2Ga_9 [31], β-Al_3Mg_2 [32], $Cd_2Re_2O_7$ [33], etc. However, most of them are conventional *s*-wave full-gap superconductors with dominant spin-singlet Cooper pairs. Time-reversal symmetry breaking is a unique feature of specific complex order parameters in noncentrosymmetric superconductivity and has been reported only for a few compounds such as Li_2Pt_3B [34] and $LaNiC_2$ [35]. In these compounds (Li_2Pt_3B and $LaNiC_2$), superconductivity occurs under ambient pressure and its T_c is

*Corresponding author: isobe.masaaki@nims.go.jp

a little higher than those of the f electron systems. However, unusually high H_{c2} beyond the Pauli limit, such as in the cerium compounds, has not been reported. It is, therefore, important to find new types of unconventional f-electron-free superconductors for further progress in understanding noncentrosymmetric physics.

The 5d transition-metal compounds, a good starting group, have the further materials design of novel noncentrosymmetric superconductors. Asymmetric spin-orbit coupling (ASOC) is a key factor for modification of the electronic structure through spin splitting. Heavy elements with unfilled d orbitals such as platinum-group elements—Pt, Ir, and Os, etc.—should be good candidates as constituent elements in noncentrosymmetric superconductors; they can induce large SOC owing to its orbital anisotropy and large relativistic effect between nuclei and electrons. In addition, a highly distorted local structure in a noncentrosymmetric crystal yields a large ligand field, resulting in large ASOC. The narrow bandwidth of the d electrons is also advantageous to enhance the noncentrosymmetric features through a slow Fermi velocity. Si may be a suitable element as a partner to the platinum-group elements—Si often reacts with Pt, Ir, or Os to form a variety of silicide intermetallics. The energy levels of the 3p and 5d orbitals are close together so the orbitals are well hybridized and often result in unfilled metallic bands near the chemical potential. The high-pressure technique of gigapascal order is a powerful method to realize chemical synthesis of new compounds. It enables us to obtain new types of dense materials that are stable under high pressure through free-energy gain, accompanied with volume shrinkage of the materials.

As a result of the search for new 5d electron system noncentrosymmetric superconductors, we recently discovered a barium-iridium silicide $BaIrSi_2$ by utilizing the high-pressure synthesis technique. We found that the compound has a unique crystal structure with a noncentrosymmetric space group and also exhibits a superconducting transition at ∼6 K. In this paper, we report details of the crystal structure and the superconducting properties, as well as the electronic structure computed using density functional theory (DFT). Based on the measurement and calculation results, we discuss the superconducting state of the noncentrosymmetric 5d electron system $BaIrSi_2$.

II. EXPERIMENTAL

We prepared polycrystalline samples of $BaIrSi_2$ using the solid-state reaction method with the high-pressure synthesis technique of gigapascal order. The starting reagents, $BaSi_2$ (2N) and Ir (3N), powders were mixed in an agate mortar at a molar ratio of 1:1, respectively, and pressed into a columnar shape of a size 6.9 mm in diameter and ∼4 mm in thickness (weight: ∼500 mg) in a glovebox filled with dry argon gas. The pellets were put in a high-pressure cell, and then reacted at 1600 °C for 1 h under 6 GPa using a flat-belt-type high-pressure apparatus, followed by quenching to room temperature before pressure release.

Phase purity and crystal structure of the products were studied using conventional powder x-ray diffraction (XRD). The XRD data were collected at room temperature using a diffractometer (Rigaku, SmartLab3) equipped with a Cu K_α radiation source and a conventional slit system. The atomic composition of crystal grains in the ceramic sample was determined using a field-emission electron probe microanalyzer (EPMA; JEOL, JXA-8500F) operated at 15 kV; $BaAl_4$, Ir, and Si were used as the standard materials. Crystal structure of $BaIrSi_2$ was observed using a high-resolution scanning transmission electron microscope (STEM; FEI, Titan Cubed) operating at 300 kV, equipped with a spherical aberration (Cs-) corrector (CEOS GmbH, DCOR). Custom software to improve the signal to noise ratio of STEM images was used [36]. The structural parameters were refined using the x-ray Rietveld method with the analysis software RIETAN-FP [37]. Electrical resistivity was measured with the standard dc four-probe method with an excitation current of ∼5 mA using a commercial apparatus (Quantum Design, PPMS). The sample geometry parameters are typically ∼4.6 mm^2 for a cross section and ∼0.5 mm in length between the voltage electrodes. Specific heat was measured for a small bulk specimen (weight: ∼9 mg) with the time-relaxation method using the PPMS. Static magnetic data were collected for a pulverized sample (weight: ∼100 mg) using a superconducting quantum interference device magnetometer (Quantum Design, MPMS).

The *ab initio* electronic structure calculations were performed by means of the full-potential linearized augmented plane-wave method using the WIEN2K software package [38]. The generalized gradient approximation [39], based on the DFT [40], was employed as the exchange-correlation energy functional. The spin-orbit interaction is included as a perturbation to the scalar-relativistic equations. Experimental lattice parameters and atomic coordinates were used for the calculation. The muffin-tin sphere radii (R) were chosen as 2.5 a.u. for Ba, 2.4 a.u. for Ir, and 2.0 a.u. for Si. The self-consistent calculations were well converged with the wave-number cutoff parameter K, satisfying $R_{\min} \times K = 7$, where $R_{\min}$ is the smallest muffin radius 2.0 a.u. The Brillouin-zone (BZ) integration for self-consistent calculations was approximated by a tetrahedron method with the BZ divided into 20 × 20 × 18 uniform mesh, which results in 990 k points in the irreducible Brillouin zone (IBZ). For density of states (DOS) and the Fermi-surface plot, eigenenergies were computed using up to 28 × 28 × 24 mesh, consisting of 2743 k points in the IBZ.

III. RESULTS AND DISCUSSION

A. Crystal structure

Figure 1(a) shows a powder XRD profile of the product sample. Almost all the Bragg reflections in the XRD profile can be indexed to a C-centered orthorhombic system of the lattice parameters $a = 15.0492(1)$ Å, $b = 8.0311(1)$ Å, and $c = 8.0314(1)$ Å. Extinctions of the reflections are $h + k = 2n$ for hkl, $k = 2n$ for $0kl$, $h = 2n$ for $h0l$, $h + k = 2n$ for $hk0$, $h = 2n$ for $h00$, $k = 2n$ for $0k0$, and $l = 2n$ for $00l$. Possible space groups are, therefore, only noncentrosymmetric $C222_1$ (no. 20). Most of the Bragg peaks are assignable to the single majority phase, indicating that the product is almost monophasic. The impurity level of secondary phases

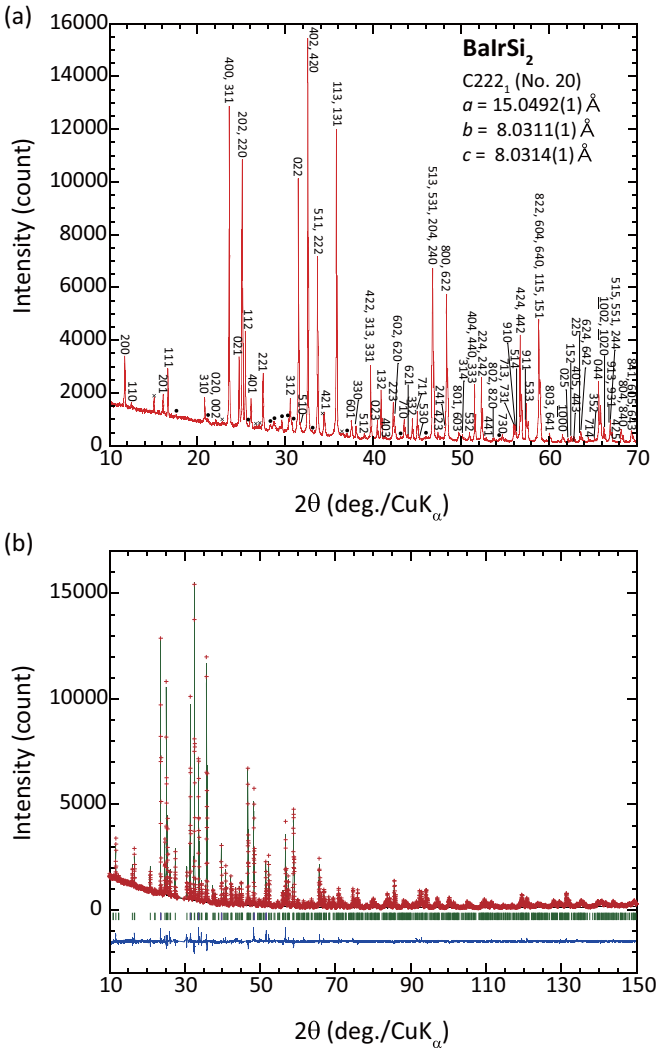

FIG. 1. (a) Powder x-ray-diffraction pattern of the $BaIrSi_2$ sample. The indices *hkl* are assigned for $BaIrSi_2$, an orthorhombic system with the space group $C222_1$ and lattice parameters $a = 15.0492(1)$ Å, $b = 8.0311(1)$ Å, and $c = 8.0314(1)$ Å. The closed circles and crosses are indications of the secondary phases: •, Ba_2SiO_4; ×, unidentified phase(s). (b) X-ray Rietveld analysis profile for $BaIrSi_2$: observed data (red crosses), calculated profile (green solid line), and its differences (blue solid line). The vertical tick marks indicate 2θ of the Bragg reflections for $BaIrSi_2$. Reliability (R) factors are $R_{WP} = 7.51\%$, $R_B = 1.71\%$, $R_F = 0.92\%$, and $S = R_{WP}/R_e = 1.604$. Some impurity Bragg peaks, e.g., $2\theta = 28$–30° for Ba_2SiO_4, are excluded from the analysis to improve the R factors. Refined structural parameters are summarized in Table I.

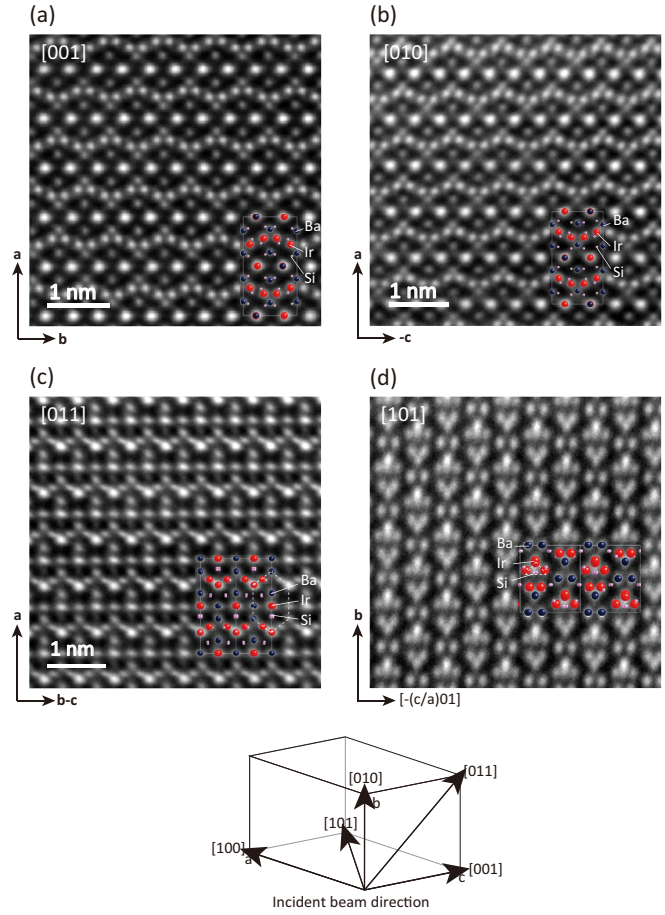

FIG. 2. STEM-ADF images for $BaIrSi_2$, projected along the (a) [001], (b) [010], (c) [011], and (d) [101] directions.

[Ba_2SiO_4 and unknown phase(s)] is less than a few percent of the main phase ($BaIrSi_2$) in intensity.

Atomic composition of the main phase was confirmed using the EPMA method with scanning electron microscopy. Backscattered electron image observation of a cleavage surface of the ceramic sample revealed that the sample is almost filled with many crystal grains showing the same brightness with a single composition. The atomic composition was measured for selected ten crystal grains of the majority phase in the ceramic sample. The average molar ratio of Ba : Ir : Si [= 25.1(2) : 24.3(1) : 50.6(4) at. %] is nearly 1:1:2, indicating that the main phase is $BaIrSi_2$. To the best of our knowledge, neither $BaIrSi_2$ nor its analogous compounds with such a unit-cell size, similar XRD pattern, and the same space group have been reported.

The crystal structure of $BaIrSi_2$ was studied using STEM. Figures 2(a)–2(d) are annular dark-field (ADF) images taken along the [001], [010], [011], and [101] directions, respectively. The atomic arrangement pattern gives the periodicity of the orthorhombic unit cell, $a \sim 1.5$ nm, $b \sim 0.8$ nm, and $c \sim 0.8$ nm, in agreement with the results of the x-ray diffraction. Ir and Ba atoms are clearly observable as bright spots in all the images, while Si atoms are dark and inconspicuous in the images. In fact, in Figs. 2(a) and 2(b), Si atoms are invisible because they are situated beside prominent spots of Ba and Ir atoms. Nevertheless, in Figs. 2(c) and 2(d), Si atoms are barely visible as obscure spots. In Fig. 2(c), dim spots (Si) are situated at one of the three inline atoms (Ba-Ir-Si) in the hexagonal pattern. Also, in Fig. 2(d), obscure spots (Si) are detectable in triangles of the prominent Ir atoms. For these images [Figs. 2(c) and 2(d)], Si atoms are superimposed on each other as a line along the projection direction to amplify its spot intensity. It was also observed that in Fig. 2(c) the atomic arrangement is vertically asymmetric, suggesting that there is no mirror plane perpendicular to the a axis in the

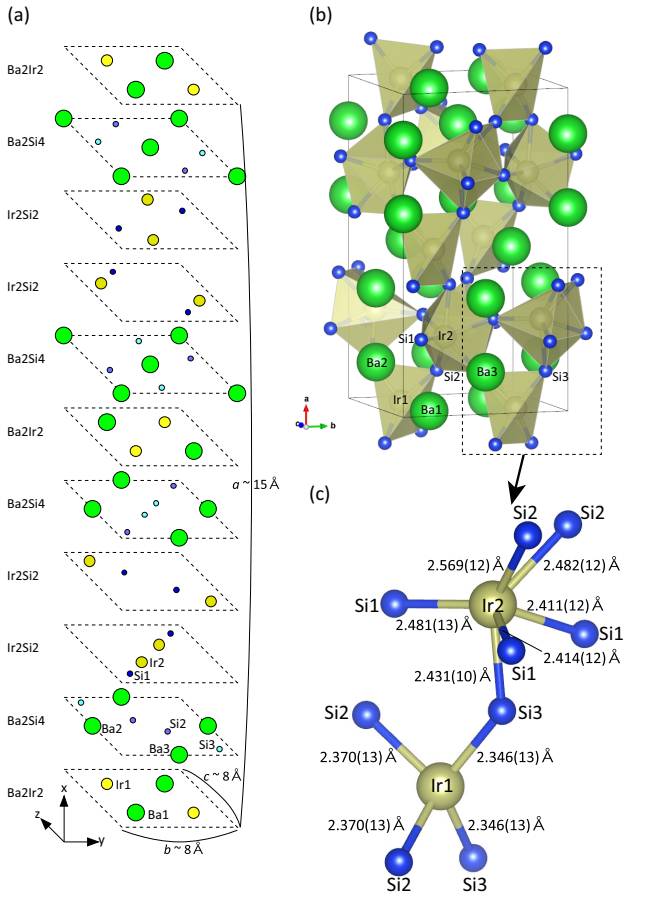

FIG. 3. (a) Schematic representation of the crystal structure model of $BaIrSi_2$, illustrated as a stack of each atomic layer along the a axis. (b) Illustration of the crystal structure of $BaIrSi_2$, depicted using the refined atomic coordinates. (c) Ir-Si bond-lengths in the Si_4(Ir1) tetrahedron and the Si_6(Ir2) octahedron.

crystal symmetry. This demonstrates the noncentrosymmetric structure of $BaIrSi_2$.

The crystal structure model of $BaIrSi_2$ was assembled to satisfy the atomic arrangement observed in the STEM images, with the symmetry space group $C222_1$. Figure 3(a) is a schematic representation of the structure, illustrated as a stack of each atomic layer along the a axis. The structural parameters were refined by Rietveld analysis using the XRD data. The best refinement x-ray Rietveld profile is shown in Fig. 1(b). Resultant reliability factors $R_{WP} = 7.51\%$, $R_B = 1.71\%$, $R_F = 0.92\%$, and $S = R_{WP}/R_e = 1.604$ are satisfactorily low. The observed XRD pattern is well reproduced by the analysis with the proposed structure model. The refined structure parameters are summarized in Table I. Figure 3(b) is an illustration of the crystal structure of $BaIrSi_2$, depicted using the refined atomic coordinates. The structure accommodates two kinds of Si polyhedrons surrounding Ir atoms. Coordination of the Ir-Si_4 tetrahedron and the Ir-Si_6 octahedron is highlighted with the Ir-Si bond lengths in Fig. 3(c). These polyhedrons are distorted, forming an asymmetric crystal field around the Ir atoms and presumably giving rise to antisymmetric spin-orbit coupling.

$BaIrSi_2$ exhibits orthorhombic symmetry. The lattice parameters are, however, almost the same for the b and c axes, i.e., $b \sim c \sim 8.03$ Å. We found that the stacking fault with the b-c plane, 90° rotation, occurs partly in the crystal. Figure 4(a) is a STEM-ADF image projected along the direction perpendicular to the a axis. The atomic arrangement pattern changes beyond the boundary line, at which the projection direction is switched from the b axis to the c axis, or vice versa [see also Figs. 2(a) and 2(b)]. Figure 4(b) is a wide view of the ADF image. The planar defect boundary appears every 30–40 × $a/2$ structure units of a single domain. The emergence ratio of the b- and c-axes projection patterns is almost equivalent.

Figure 5(a) are ADF and annular bright-field (ABF) images projected along the [100] direction for a single domain sample. In the ADF image, the zigzag chain is clearly observable as sequential prominent spots of heavy elements (Ba and Ir) running toward the c direction. In contrast, in the ABF image, light elements (Si) bridging the zigzag chains are somewhat more emphasized than those in the ADF image because of atomic number dependence of ABF images [41]. Figure 5(b) shows wide views of the ADF and ABF images projected along the [100] direction. In these images, the right area is for the thin part of the sample with a single domain, while the left area is for the thick part of the sample at which plural domains overlap through the projection direction (a axis). In the left area, the zigzag chain is undistinguishable because the c axis mixes with the b axis in the projection direction. As a result, the STEM images demonstrate the proposed crystal structure of $BaIrSi_2$, in particular for atomic positions of Si.

B. Superconducting properties

$BaIrSi_2$ shows superconductivity at low temperature. Figure 6(a) shows the temperature (T) dependence of the electrical resistivity under the magnetic fields $\mu_0 H = 0$ and 5.5 T. A superconducting transition occurs at the critical temperature $T_c \sim 6$ K at zero field, while the superconductivity disappears under $\mu_0 H = 5.5$ T. In the normal state ($T > T_c$), T dependence of the resistivity exhibits metallic behavior like a Bloch-Grüneisen type. No magnetoresistance was observed. The large residual resistivity ($\rho_0 \sim 0.53$ mΩ cm) and rather low relative resistance ratio ($\rho_{300K}/\rho_0 \sim 3.8$) suggest that impurity and/or lattice-imperfection scattering is dominant at least around low temperatures for the electrical resistivity. In addition, grain-boundary scattering in the polycrystalline sample and semimetallicity also might be contributions to them. These imply the short mean free path l. Figure 6(b) shows T dependence of electrical resistivity below 8 K under various magnetic fields between 0 and 5.5 T. When $\mu_0 H = 0$, the onset $T_c(= T_c^{onset})$ is ~6.4 K, and the zero-resistivity $T_c(= T_c^0)$ is ~5.9 K. Application of the magnetic fields gradually suppresses the superconductivity. At $\mu_0 H = 5.5$ T, the superconducting transition is almost invisible at 1.9 K.

Magnetic data for the superconducting transition of $BaIrSi_2$ are shown in Fig. 7. Panel (a) shows the T dependence of magnetic susceptibility χ ($\sim M/H$). The data were collected for a powder sample under $\mu_0 H = 1$ mT in the heating process after zero-field cooling (ZFC) and then sequentially in field cooling (FC). The diamagnetic signals due to a superconducting transition appear below ~6 K (onset T_c). The bulk

TABLE I. Atomic coordinates (x, y, z), isotropic displacement parameters B, and crystallographic data of $BaIrSi_2$.

Atom	Site	g[a]	x	y	z	B(Å^2)
Ba1	4*b*	1	0	0.2405(4)	1/4	0.45(6)
Ir1	4*b*	1	0	0.2344(3)	3/4	0.50(5)
Ba2	4*a*	1	0.1413(3)	0	1/2	0.69(7)
Ba3	4*a*	1	0.1299(2)	1/2	0	0.60(7)
Ir2	8*c*	1	0.22021(10)	0.3787(4)	0.3755(4)	0.43(3)
Si1	8*c*	1	0.2277(7)	0.1608(15)	0.1571(15)	−0.64(18)
Si2	8*c*	1	0.1025(5)	0.5944(19)	0.3944(17)	0.05(17)
Si3	8*c*	1	0.1188(6)	0.905(2)	0.122(3)	0.22(20)
Formula (asymmetric structure unit)		$Ba_3Ir_3Si_6$				
Molecular weight		1157.145				
Space group		$C222_1$ (no. 20)				
Lattice constants		$a = 15.04920(13)$ Å, $b = 8.03119(11)$ Å, $c = 8.03144(11)$ Å, $V = 970.709(20)$ Å^3				
Z		4				
Density (calculated)		7.9178 g/cm^3				
Temperature		Room temperature				
Wavelength		1.540593 Å (Cu K_α)				
R factors		$R_{WP} = 7.51\%$, $R_p = 5.48\%$, $R_B = 1.71\%$, $R_F = 0.92\%$, $S = R_{WP}/R_e = 1.604$				
Refinement software		RIETAN-FP				

[a]Occupancies for all the atoms are fixed to 1: $g = 1$.

T_c is around 5.8 K, below which the signal rapidly increases. The magnetic susceptibility value for the ZFC shielding effect at 1.8 K is -9.4×10^{-3} emu/g($= -7.4 \times 10^{-2}$ emu/cm^3), which corresponds to about 93% of the full-volume Meissner signal $-1/4\pi$ [42]. The large signal ensures that the observed superconductivity is a bulk phenomenon originating from the main phase $BaIrSi_2$ in the sample. Panel (b) shows an M-H hysteresis curve for the superconducting state at 1.8 K. The data were taken after ZFC from a temperature above T_c. The behavior of the M-H curve is of type-II superconductors.

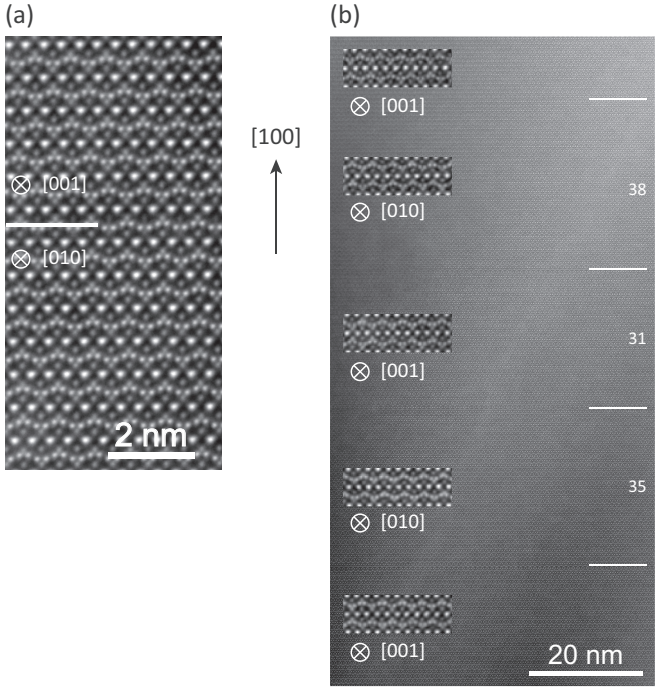

FIG. 4. (a) STEM-ADF image projected along the direction perpendicular to the a axis. The lateral line indicates a domain boundary at which the projection direction is switched from the b axis to the c axis, and vice versa. (b) Wide view of the ADF image. The domain boundary appears every 30–40 × a/2 structure units along the a axis.

Specific-heat (C_p) data for $BaIrSi_2$ are plotted as C_p/T versus T^2 in Fig. 8(a). The data were collected on cooling to 1.9 K under several magnetic fields between $\mu_0 H = 0$ and 7 T. The magnetic fields were applied above T_c before each measurement. When $\mu_0 H = 0$, a superconducting transition with a specific-heat jump was observed around $T_c^{\text{onset}} \sim 6.3\,\text{K}(T^2 \sim 39.7\,\text{K}^2)$. Superconductivity is gradually suppressed with $\mu_0 H$, and completely vanishes at 7 T. At a low-temperature limit, the specific heat for the normal state can be expressed as

$$C_p \sim C_v = \gamma T + \frac{12\pi^4}{5} r N_A k_B \left(\frac{T}{\Theta_D}\right)^3, \qquad (1)$$

where γ, Θ_D, N_A, k_B, and r denote the Sommerfeld constant, Debye temperature, Avogadro number, Boltzmann constant, and number of atoms per molecule, respectively. From the linear extrapolation of the $\mu_0 H = 7\,\text{T}$ dataset at low temperatures ($T < 3\,\text{K}$), we estimated $\gamma \sim 5.7\,\text{mJ/mole K}^2$ and $\Theta_D \sim 305\,\text{K}$. The range of γ suggests a conventional Fermi-liquid behavior with little effective-mass enhancement for electron correlation. Phonon mediation seems to be dominant for Cooper pairing in $BaIrSi_2$.

The electronic part of the specific heat C_{el} in the superconducting state under each magnetic field was obtained by subtracting the lattice part of the normal-state specific heat from the raw data. Figure 8(b) shows C_{el}/T versus T plots under the various magnetic fields. By idealizing the specific-heat jump to ensure entropy balance around the transition, the bulk thermodynamic critical temperature $T_c(= T_c^{\text{bulk}})$ was determined for each dataset taken under the magnetic field.

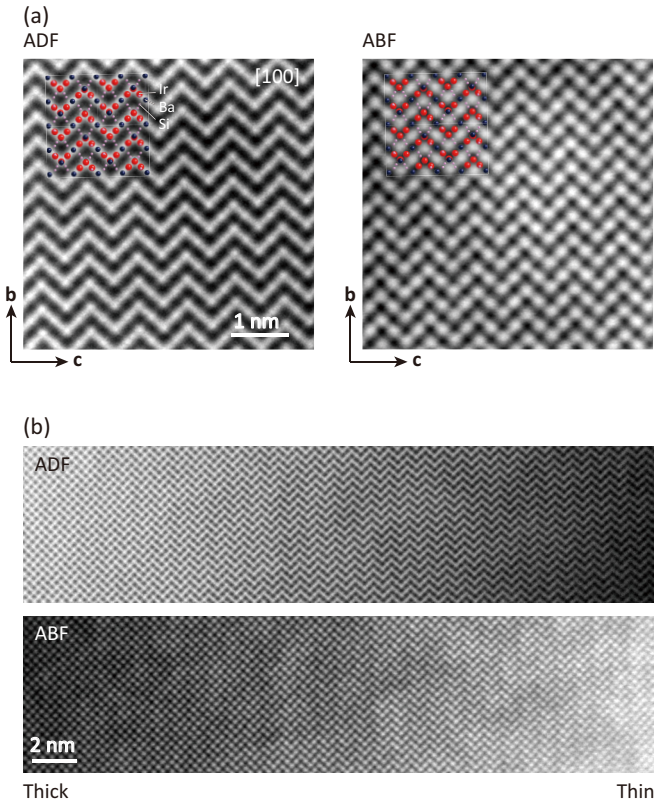

FIG. 5. (a) ADF and ABF images projected along the [100] direction for a single domain sample. The zigzag atomic arrays of Ba and Ir run for the [001] direction. (b) Wide views of the ADF and ABF images. The right area in the image is for the thin part of the sample with a single domain, while the left area is for the thick part with overlapping plural domains through the [100] projection direction.

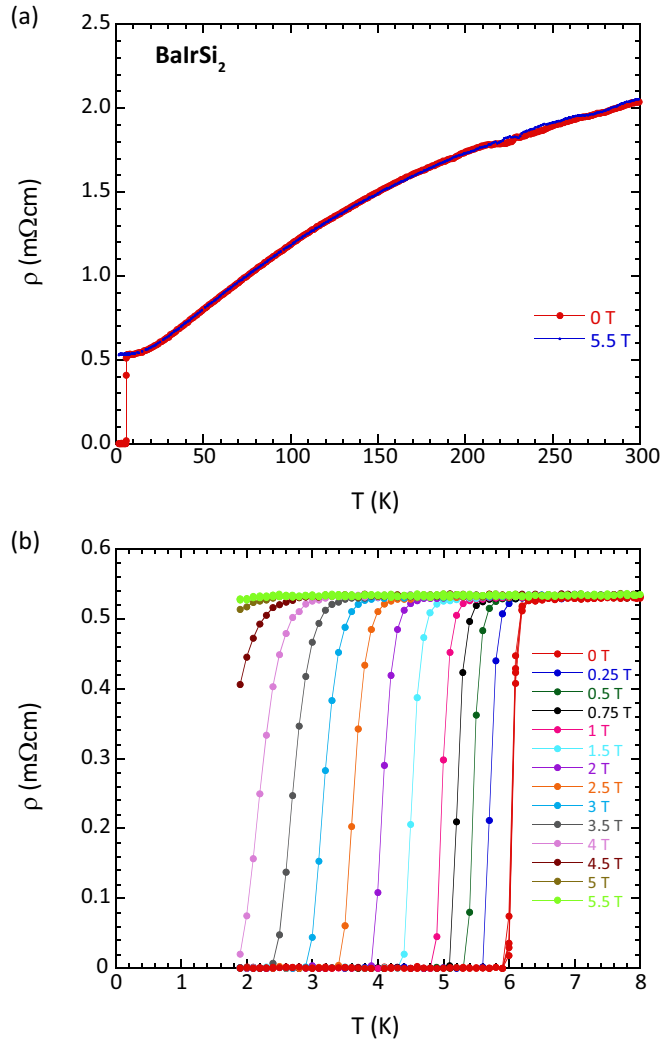

FIG. 6. Temperature (T) dependence of electrical resistivity (ρ) for a $BaIrSi_2$ polycrystalline sample. (a) Data taken in the wide temperature range of $1.9 \leqslant T \leqslant 300$ K under the magnetic fields $\mu_0 H = 0$ and 5.5 T. Superconductivity occurs at $T_c \sim 6$ K under $\mu_0 H = 0$. (b) Field response of the superconducting transition as measured at various externally applied magnetic fields. The superconductivity is suppressed by the magnetic field, and disappears around $\mu_0 H \sim 5.5$ T.

When $\mu_0 H = 0$, $T_c^{\rm bulk}$ is 5.8 K. The Sommerfeld constant γ principally consists of the γ_n term attributed to the superconducting phase being in the normal state at $H > H_{c2}$, and γ may also include a correction term γ_0 due to extrinsic nonsuperconducting metallic phase(s) in the sample, i.e., $\gamma = \gamma_n + \gamma_0$. The γ_0 value was estimated to be $\sim$0.2 mJ/mole K^2, i.e., $\gamma_n \sim 5.5$ mJ/mole K^2, so that the conservation of entropy is satisfied between the normal state (at $\mu_0 H = 7$ T) and the superconducting state (at $\mu_0 H = 0$ T), i.e., $\gamma_n T_C = \int_0^{T_C} \frac{C_{\rm el}}{T} - \gamma_0 dT$. At $\mu_0 H = 0$, the magnitude of the idealized specific-heat jump at $T_c^{\rm bulk}$ is $\Delta C_{\rm el}/T_c \sim 9.1$ mJ/mole K^2, giving the normalized specific-heat jump as $\Delta C_{\rm el}/\gamma_n T_c \sim 1.65$. This value is slightly greater than the value of 1.43 for a BCS prediction. This suggests that $BaIrSi_2$ can be regarded as an intermediate-coupling superconductor, in which electron-phonon interaction is moderately enhanced as compared to the conventional BCS weak-coupling superconductors. The measured superconducting properties compare favorably with the following strong-coupling corrections [43–46]:

$$\left[\frac{\Delta C_{\rm el}}{\gamma_n T_c}\right]_{T_c} = 1.43\left[1 + 53\left(\frac{T_c}{\omega_{\ln}}\right)^2 \ln\left(\frac{\omega_{\ln}}{3T_c}\right)\right], \quad (2)$$

$$\frac{2\Delta_0}{k_B T_c} = 3.53\left[1 + 12.5\left(\frac{T_c}{\omega_{\ln}}\right)^2 \ln\left(\frac{\omega_{\ln}}{2T_c}\right)\right], \quad (3)$$

$$\frac{\gamma_n T_c^2}{H_c(0)^2} = 0.168\left[1 - 12.2\left(\frac{T_c}{\omega_{\ln}}\right)^2 \ln\left(\frac{\omega_{\ln}}{3T_c}\right)\right], \quad (4)$$

$$T_c = \left(\frac{\omega_{\ln}}{1.2}\right)\exp\left[-\frac{1.04(1+\lambda_{ep})}{\lambda_{ep} - \mu^*(1+0.62\lambda_{ep})}\right], \quad (5)$$

where $\omega_{\ln}$ is a characteristic phonon temperature defined as the logarithmic moment of the electron-phonon spectral function $\alpha^2 F(\omega)$ and μ^* is a Coulomb pseudopotential parameter. We first determined $\omega_{\ln} \sim 160$ K using experimentally measured $\Delta C_{\rm el}/\gamma_n T_c (= 1.65)$ and $T_c (= T_c^{\rm bulk} = 5.8$ K) with Eq. (2), then obtained $2\Delta_0/k_B T_c \sim 3.68$,

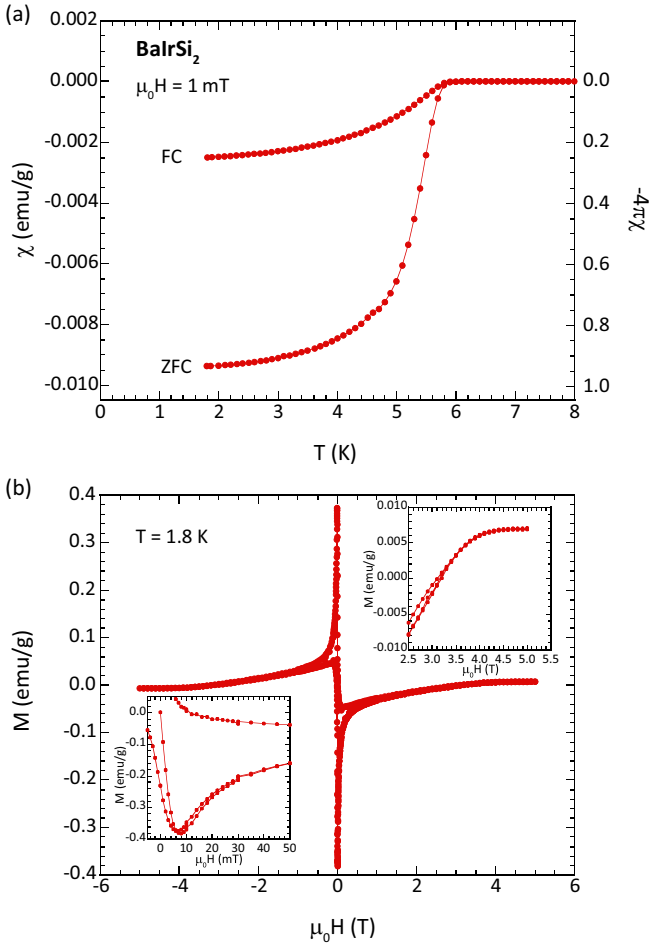

FIG. 7. (a) Temperature dependence of magnetic susceptibility χ ($\sim M/H$) for $BaIrSi_2$. The data were collected for a powder sample under $\mu_0 H = 1$ mT in the heating process after zero-field cooling and field cooling. (b) Magnetization curve (M-H hysteresis curve) for the superconducting state at 1.8 K. Inset: Magnifications of the low- and high-magnetic-field regions.

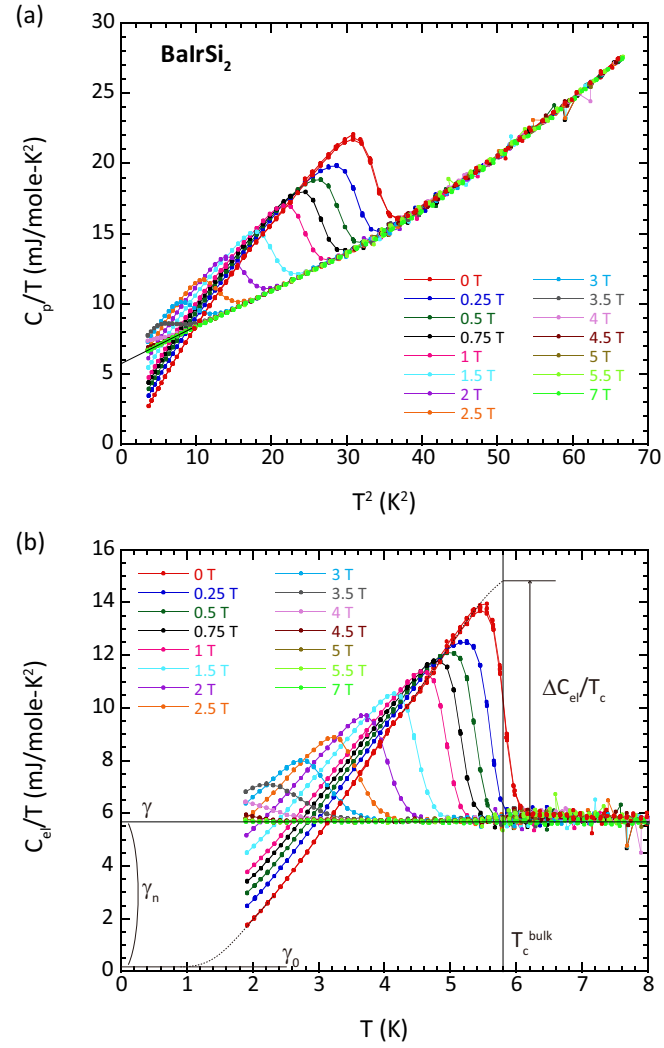

FIG. 8. Specific heat for $BaIrSi_2$, measured under various magnetic fields between $\mu_0 H = 0$ and 7 T. (a) C_p/T vs T^2 plots, where C_p is the measured value. The Sommerfeld constant ($\gamma = 5.7\,\mathrm{mJ/mole\,K^2}$) and Debye temperature ($\Theta_D = 305$ K) were determined from the low-temperature linear extrapolation of the $\mu_0 H = 7$ T specific-heat curve. (b) Electronic specific heat C_{el}/T vs T plots. The vertical line gives a bulk thermodynamic critical temperature $T_c^{bulk} = 5.8$ K at $\mu_0 H = 0$, while the horizontal line indicates γ. $\gamma = \gamma_n + \gamma_0$, where $\gamma_n (\sim 5.5\,\mathrm{mJ/mole\,K^2})$ is the main component attributed to the superconducting phase being in the normal state at $H > H_{c2}$, and $\gamma_0 (\sim 0.2\,\mathrm{mJ/mole\,K^2})$ is a correction term due to extrinsic nonsuperconducting metallic phase(s) in the sample. The normalized specific-heat jump is $\Delta C_{el}/\gamma_n T_c \sim 1.65$.

$\gamma_n {T_c}^2/{H_c(0)}^2 \sim 0.162$ [i.e., $\mu_0 H_c(0) \sim 48$ mT], and $\lambda_{ep} \sim 0.8$ using the ω_{ln} value and the standard μ^* value ($= 0.13$) [47] with Eqs. (3), (4), and (5), respectively. The value $T_c/\omega_{ln} \sim 0.036$ reasonably satisfies the condition $T_c/\omega_{ln} \ll 1$, applicable to the formulas.

The electronic specific heat of the superconducting phase C_{el}'($= C_{el} - \gamma_0 T$) was obtained by multiplying the $C_{el}/T - \gamma_0$ dataset by each temperature. Figure 9(a) shows C_{el}' versus T plots for various magnetic fields. In general, in a superconducting state, heat is carried by thermally excited quasiparticles. The low-temperature excitation of the electronic specific heat directly reflects its gap structure in the superconducting order parameter. For example, uniform-gap (isotropic-gap) structure gives thermal-activation-type temperature dependence of the specific heat, i.e., $C_{el}' \propto \exp(-\Delta/k_B T)$, while for a line-nodal-gap (anisotropic-gap) state specific heat is predicted to be proportional to T^2, i.e., $C_{el}' \propto T^2$, at low temperatures [48]. Figure 9(b) (main panel) shows the $\mu_0 H = 0$ data of the T-dependent electronic specific heat $C_{el}'(T)$ in the superconducting state ($T < T_c$) for $BaIrSi_2$, where C_{el}' and T are normalized by $\gamma_n T_c$ and T_c, respectively. The solid curve represents T dependence of C_{el}' for ideal weak-coupling BCS uniform-gap-type superconductors using Mühlschlegel's model [49], which is expected to be more appropriate for the high-temperature range $0.5 < T/T_c < 1.0$ than for lower temperatures. In $BaIrSi_2$ enhanced electron-phonon coupling results in a slightly lifted $C_{el}'(T)$ data line in the high-temperature range $0.7 < T/T_c < 1.0$, as compared to the theoretical curve. $C_{el}'(T)$ is rapidly attenuated with decreasing T, and almost disappears around $T \sim 0.2 T_c$. The

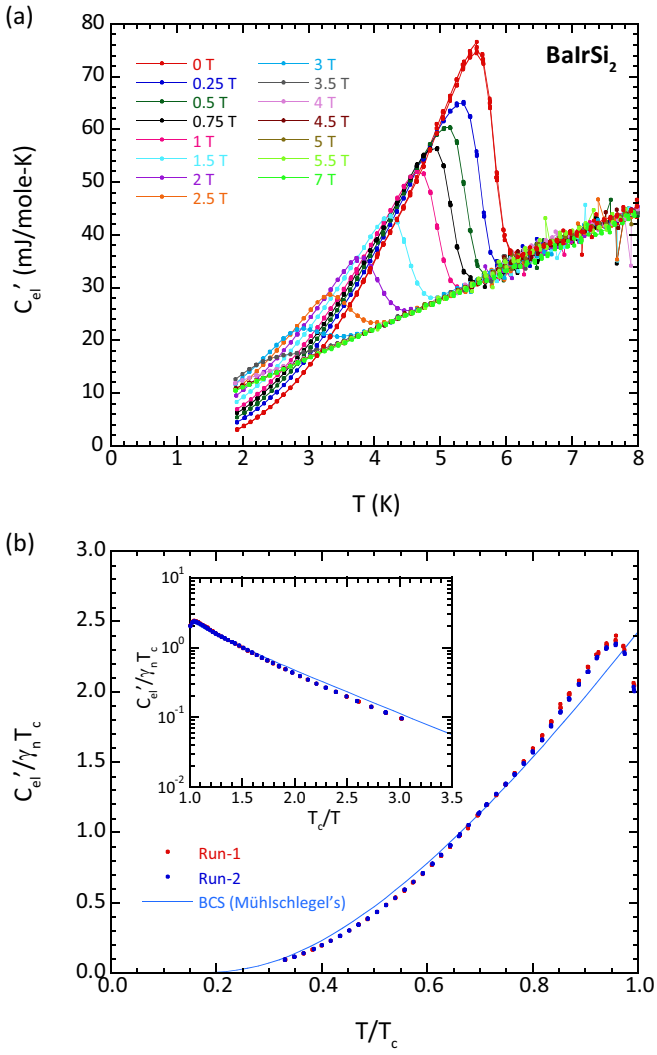

FIG. 9. (a) Electronic specific heat of the superconducting phase $C_{\rm el}$' vs T plots under the various magnetic fields. (b) Dependence of the reduced electronic specific heat $C_{\rm el}'/\gamma_n T_c$ on the reduced temperature T/T_c at $\mu_0 H = 0$ in the superconducting state ($T/T_c < 1$) for $BaIrSi_2$. The solid line represents the theoretical curve for weak-coupling BCS superconductors by Mühlschlegel's model [49]. The inset in panel (b) shows a semilogarithmic plot of the reduced electronic specific heat vs inverse reduced temperature.

inset of Fig. 9(b) shows a semilogarithmic plot of the reduced electronic specific heat $C_{\rm el}'/\gamma_n T_c$ versus inverse reduced temperature T_c/T. The behavior appears as an activated T dependence with a full-gap (nodeless-gap) character, suggesting possible dominant spin-singlet s-wave Cooper pairing in $BaIrSi_2$. However, on a closer look, the data line is not straight and gently curves on this plot; the gradient of $C_{\rm el}'(T)$ is reduced with decreasing T in $T_c/T > 2.0$. In the main panel of Fig. 9(b), the data line evidently reduces its attenuation rate around the measured lowest temperature 1.9 K. It seems that the data-line shape is more nearly consistent with two-gap superconductivity than uniform single-gap superconductivity. Precise measurements at lower temperatures are necessary to better understand the superconducting-gap structure in $BaIrSi_2$.

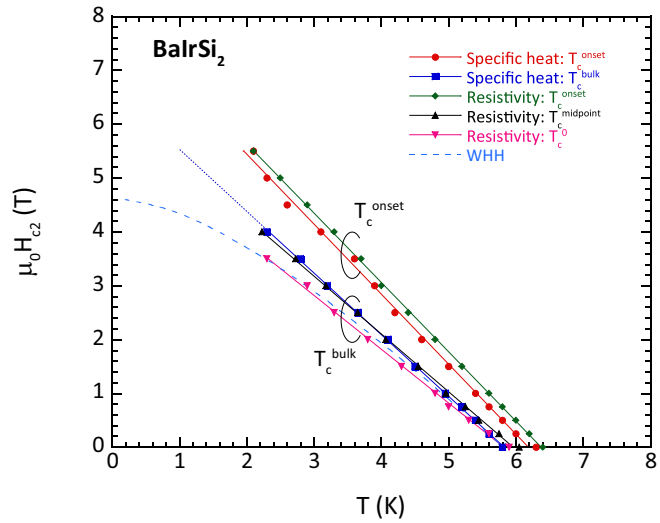

FIG. 10. Upper critical field $\mu_0 H_{c2}$ plotted as a function of T. The data points are given by the transition temperatures $T_c^{\rm bulk}$ and $T_c^{\rm onset}$ for the electrical resistivity [Fig. 6(b)] and the electronic specific heat [Fig. 8(b)]. The dotted lines indicate linear extrapolation of the $T_c^{\rm bulk}$ data line to $T = 0$ K for electronic specific heat, and the broken line indicates the theoretical $\mu_0 H_{c2}(T)$ curve for dirty-limit BCS weak-coupling superconductors given by Werthamer-Helfand-Hohenberg [54,55].

Figure 10 summarizes the relation between the upper critical field and the critical temperature of the superconducting state. In this plot, the data points of $T_c(H)$ were obtained from the plots of T-dependent electrical resistivity [Fig. 6(b)] and electronic specific heat [Fig. 8(b)] under magnetic fields. The $\mu_0 H_{c2}$ values show small dependency on the definition of T_c ($T_c^{\rm onset}$ or $T_c^{\rm bulk}$) and the method of the measurement (specific heat or resistivity) [50]. However, it seems that for any dataset line $\mu_0 H_{c2}$ tends to increase almost linearly with decreasing temperature at least within the measured temperatures; no saturation was observed even at the lowest $T (= 1.9\,{\rm K} \sim 0.3 T_c)$. It is difficult to determine the exact value of $\mu_0 H_{c2}$ at $T = 0$ K, because there are no data points near $T \sim 0$ K. However, from the extrapolation of the dataset lines, $\mu_0 H_{c2}(0)$ can be presumably expected to be within the range between 5 and 8 T. The tentative linear extrapolation of the $T_c^{\rm bulk}$ line for the specific-heat data gives a rough estimate of the upper critical field $\mu_0 H_{c2}(0) \sim 6$ T.

For type-II superconductors, the upper critical field $H_{c2}(0)$ depends on both Pauli limit H_P and orbital limit $H_{\rm orb}$. The Maki parameter α_M is defined as $\alpha_M = \sqrt{2} H_{\rm orb}/H_P$ [51,52]. The Pauli limit H_P is due to paramagnetic pair breaking and corresponds to the magnetic field at which its Zeeman splitting energy balances the superconducting condensed energy Δ_0. Accordingly, H_P can be given by

$$H_P = \frac{\sqrt{2}\Delta_0}{g\mu_B\sqrt{1-\frac{\chi_s}{\chi_n}}}, \qquad (6)$$

where g is the g value ($= 2.0$ for free electrons), μ_B is the Bohr magneton, and χ_s and χ_n are spin susceptibilities of the superconducting state and Pauli spin susceptibility at T_c in

TABLE II. Superconducting parameters for $BaIrSi_2$.

	$BaIrSi_2$
Onset critical temperature, T_c^{onset}	6.3 K
Bulk critical temperature, T_c^{bulk}	5.8 K
Thermodynamic critical field, $\mu_0 H_c(0)$	49 mT
Upper critical field, $\mu_0 H_{c2}(0)$	6 T
Ginzburg-Landau parameter, κ_{GL}	87
Coherence length, ξ_0	7.4 nm
Penetration depth, λ_0	640 nm
Specific-heat jump, $\Delta C_{\text{el}}(T_c)/\gamma_n T_c$	1.65
Characteristic phonon temperature, $\omega_{\ln}(T_c/\omega_{\ln})$	160 K (0.036)
Electron-phonon coupling constant, λ_{ep}	0.8
Superconducting gap, $2\Delta_0/k_B T_c$	3.68
Ratio of critical temperature and field, $\gamma_n {T_c}^2/H_c(0)^2$	0.162
Density of states, $N(E_F)$	6.8 state/eV f.u. (f.u.: $Ba_6Ir_6Si_{12}$)
Residual resistivity ρ_0	0.53 mΩ cm
Sommerfeld constant, γ_n	5.5 mJ/mole K^2
Debye temperature, Θ_D	305 K

the normal states, respectively [53]. For $BaIrSi_2$, assuming the spin-singlet Cooper pair [$\chi_s(0) = 0$] and $2\Delta_0/k_B T_c \sim 3.68$, the Pauli limit is tentatively estimated as $\mu_0 H_P = 1.94 \times T_c \sim 11$ T. If noncentrosymmetric superconductivity with antisymmetric spin-orbit coupling is effective, i.e., $\chi_s(0) \neq 0$, $\mu_0 H_P$ should be greater than 11 T. In any case, $\mu_0 H_P$ is beyond the observed $\mu_0 H_{c2}(0)(\sim 6\,\text{T})$, suggesting that the actual upper critical field is limited by orbital pair breaking, i.e., $H_{c2}(0) = H_{\text{orb}}$ and $\alpha_M <\sim 1/\sqrt{2}$.

Orbital limit H_{orb} is pair breaking due to Lorentz force. H_{orb} is deduced from the Ginzburg-Landau (GL) theory as

$$H_{\text{orb}} = \frac{\Phi_0}{2\pi\xi_0^2}, \tag{7}$$

where Φ_0 is the fluxoid quantum and ξ_0 is the superconducting coherence length. According to the Werthamer-Helfand-Hohenberg (WHH) theory for conventional weak-coupling BCS-type superconductors, the T-dependent $H_{c2}(T)$ curve draws a gradual saturation curvature with decreasing T and crosses the $T = 0$ K axis at a finite orbital limit ${H_{\text{orb}}}^{\text{BCS}}$ described as $H_{\text{orb}}^{\text{BCS}} = 0.69 \times [-(\frac{dH_{c2}(T)}{dT})|_{H=0}] \times T_c$ for a dirty limit case ($l \ll \xi$) [54,55]. For $BaIrSi_2$, the orbital limit value can be estimated around 4.6 T, if the WHH theory is applied to it. However, the observed $\mu_0 H_{c2}(T)$-T data do not fit the WHH theory curve; its T dependence rather looks like a more T-linear behavior even at lower temperatures. A similar behavior, i.e., deviation of $\mu_0 H_{c2}(T)$ from the WHH theory, has been reported also in some noncentrosymmetric compounds, such as $CaIrSi_3$ [18]. However, origin of the deviation has not yet been clear. At least, it seems impossible to explain such a deviation with the framework of the electron-phonon model with weak or intermediate coupling [56]. Presumably, for $BaIrSi_2$, there may exist a more essential mechanism such as scenarios suggested in [57,58].

Some other superconducting parameters of $BaIrSi_2$ were estimated using the specific-heat data on the assumption that the upper critical field at $T = 0$ K is approximately $\mu_0 H_{c2}(0) \sim 6$ T. The thermodynamic critical field $\mu_0 H_c(0)$ is calculable from the free-energy difference between the superconducting and normal states, given by the expression $\frac{1}{2}\mu_0 H_c^2(0) = F_n - F_s = -\frac{1}{2}\gamma_n T_c^2 + \int_0^{T_c} C_{\text{el}}(T)dT$. Numerical integration of the electronic specific heat at $\mu_0 H = 0$ gives a result of $\mu_0 H_c(0) \sim 49$ mT, which is almost in agreement with the calculated value from Eq. (3). These values were put into the formula $H_{c2}/H_c = \sqrt{2}\kappa_{\text{GL}}$ to obtain the Ginzburg-Landau parameter $\kappa_{\text{GL}} \sim 87$, supporting that $BaIrSi_2$ is a type-II superconductor. Superconducting coherence length and penetration depth were estimated to be $\xi_0 \sim 7.4$ nm and $\lambda_0 \sim 640$ nm using the formulas $\mu_0 H_{c2} = \Phi_0/2\pi{\xi_0}^2$ and $\kappa_{\text{GL}} = \lambda_0/\xi_0$, respectively. These parameters are summarized in Table II with other physical properties determined in this paper.

C. DFT electronic structure

Figure 11 is a plot of the electronic band structure of $BaIrSi_2$ in the energy range of $-8 \leqslant E \leqslant +6$ eV, for scalar-relativistic calculations without SOC [Fig. 11(a)] and relativistic calculations including SOC [Fig. 11(b)]. A close-up view of the band structure near the Fermi energy E_F ($-1 \leqslant E \leqslant +1$ eV) for each calculation is highlighted in the lower panels. The band calculation is conducted for a primitive unit cell, i.e., one-half of the conventional base-centered orthorhombic unit cell, $Ba_6Ir_6Si_{12}$. The Fermi energy E_F is set to zero. The labels Γ, X, Y, Z, T_X, and T_Y denote symmetry points in the Brillouin zone [see Fig. 13(a)]. The X and Y points are equivalent. Similarly, the T_X and T_Y points are equivalent. (The subscripts X and Y distinguish the direction in the k space.) There is a band gap at the Γ point slightly above E_F ($+0.25 \leqslant E \leqslant +0.46$ eV; $\Delta_G \sim 0.21$ eV). Near the valence-state top energy bands cross E_F, forming a metallic state in $BaIrSi_2$. This is consistent with the experimental results of the resistivity and specific-heat measurements. Numerous narrow bands exist around the upper half of the valence state, $E >\sim -5$ eV. These narrow bands are derived from Ir-5d orbitals.

To highlight the orbital origin of the band structure, the calculated partial and total electronic DOS [$N(E)$] with SOC in the energy range of $-8 \leqslant E \leqslant +6$ eV are shown in Fig. 12. The total DOS clearly exhibits the valence state

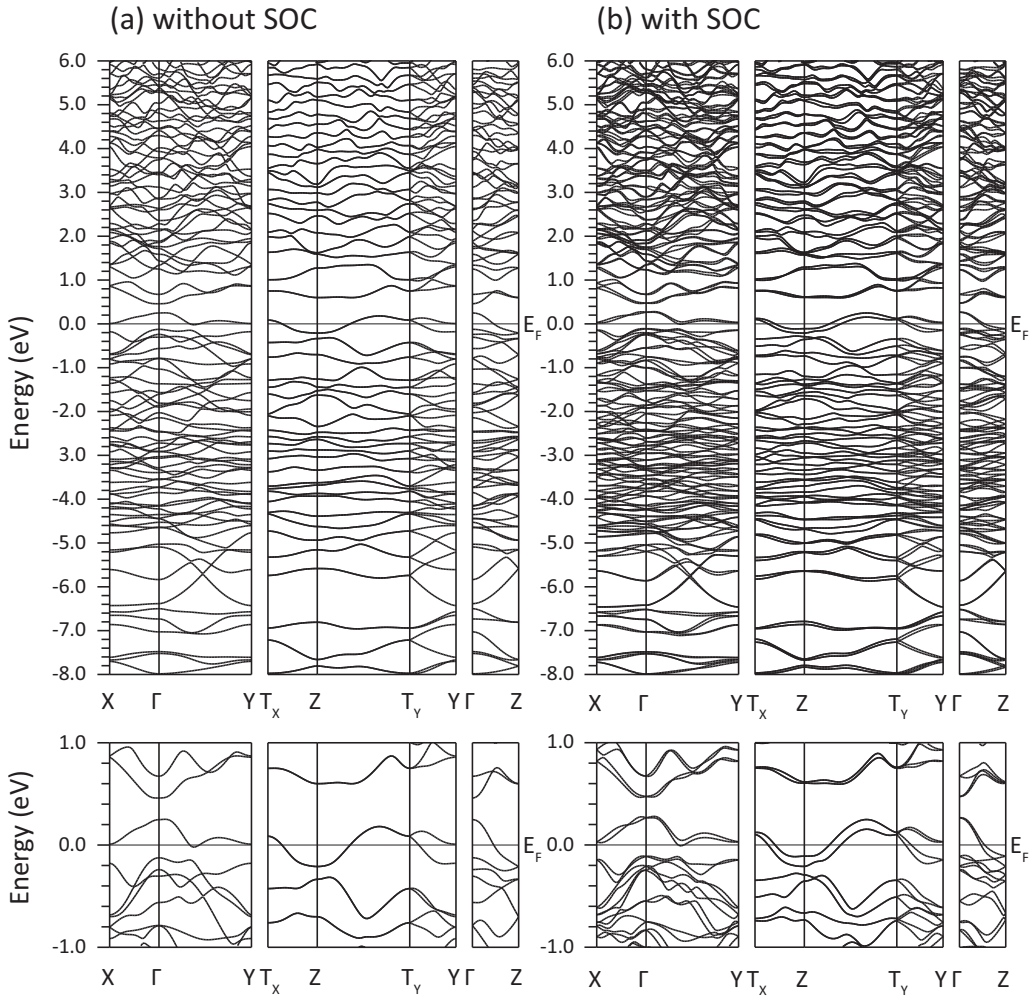

FIG. 11. Electronic band structure of $BaIrSi_2$: (a) scalar-relativistic calculations without SOC and (b) relativistic calculations including SOC. The lower panel shows close-up views of the band structure near Fermi energy E_F. The Fermi energy E_F is set to be zero. For the codes of the symmetry points (Γ, *X, Y, Z,*T_X, and T_Y) in the Brillouin zone, see Fig. 13.

(–6.5 $\leqslant E \leqslant$ +0.25 eV) and the unoccupied state ($E \geqslant$ +0.46 eV) with a band gap [$N(E) = 0$ state] intervening between them. The Fermi energy ($E_F = 0$) is situated near the top of the valence state, yielding a finite DOS at E_F. The value of the total DOS at the Fermi energy is $N(E_F) \sim 6.8$ states/eV f.u.$^{-1}$. The electronic specific-heat coefficient can be tentatively estimated from this $N(E_F)$ and an experimental electron-phonon coupling of $\lambda_{ep} \sim 0.8$ using the following equation:

$$\gamma_n^{\rm cal} = \tfrac{1}{3}\pi^2 k_B^2 N(E_F)(1+\lambda_{ep}). \quad (8)$$

The resulting value ($\gamma_n{}^{\rm cal} \sim 4.8$ mJ/mole K^2) is about 13% smaller than the measured value ($\gamma_n \sim 5.5$ mJ/mole K^2), suggesting that a small effective-mass enhancement for electronic correlation in $BaIrSi_2$ exists. The partial DOS revealed that the DOS of $BaIrSi_2$ originates in Ir, Si, and Ba orbitals in the outermost shell, widely distributed over all the energy ranges of the valence and unoccupied states. The valence state is derived mainly from Ir-5*d* and Si-3*p* bonding orbitals, while the unoccupied state mainly originates in Ba-5*d* and Ir-5*d* antibonding orbitals. In the valence state, the Ir-5*d* orbitals give prominent DOS peaks around $-5 \leqslant E \leqslant -1$ eV, due to its narrow-band character for *d* electrons. The Si-3*p* orbitals, which have a relatively wide-band character, are hybridized with the Ir-5*d* orbitals in the same energy range, forming the valence state. The valence state spreads over the energy range beyond E_F, and the edge of the hybridized orbital bands lies on E_F. In contrast, the Ba-5*d* orbitals are distributed consistently above E_F. Its contribution to $N(E_F)$ is not so large. As a result, the valence state near E_F consists of mainly the Ir-5*d* and Si-3*p* orbitals, as well as limited contribution from the Ba-5*d* orbitals.

When going back to the band structures in Fig. 11, distinctive differences can be observed between the calculations with SOC and without SOC. SOC obviously splits the degeneracy of the scalar-relativistic bands and shifts the bands in energy. Notable amounts of band splitting are observable in the band structure for the calculations with SOC. At general *k* points in the Brillouin zone, twofold spin-degenerated scalar-relativistic bands split into two subbands (bands without spin degeneracy) due to noncentrosymmetry in the crystal structure

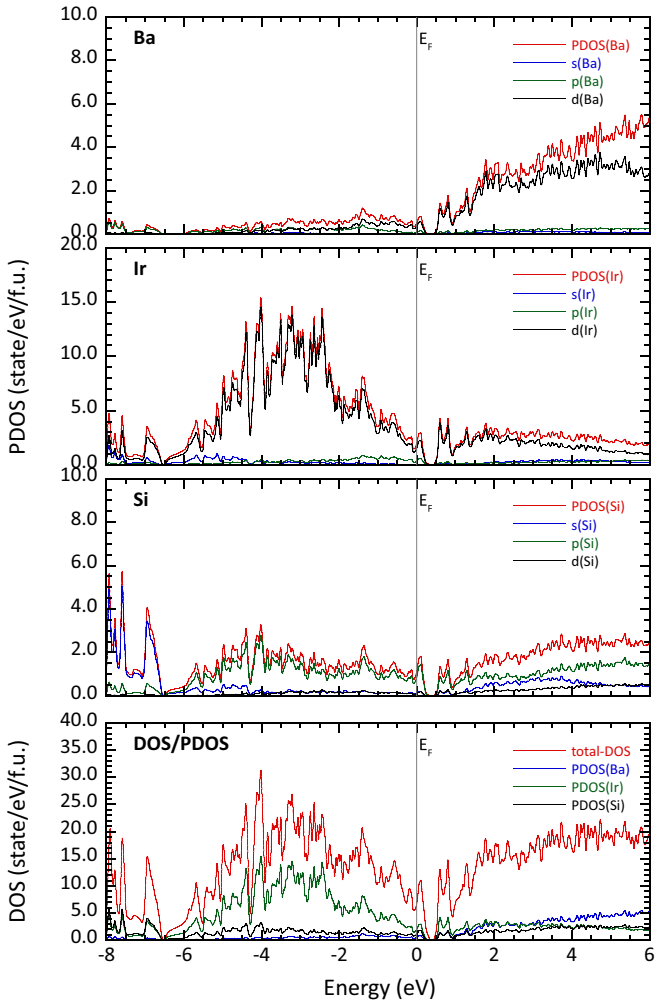

FIG. 12. Total and partial electronic density of states of $BaIrSi_2$, for the case of relativistic calculations with SOC.

after switching on SOC. Such splitting can also be seen at k points on the X-Γ-Y, T_Y-Y, and Γ-Z lines. However, at the special k points in the Brillouin-zone boundary, including the T_X–Z and T_Y–Z lines, the twofold degeneracy of bands remains even with SOC because of the crystallographic symmetry. At such special k points, the scalar-relativistic bands have additional twofold degeneracy by space-group symmetry. Namely, they are fourfold degenerated if spin degeneracy is counted. The SOC only splits them into two sets of twofold degenerated bands.

Focusing on the electronic bands near E_F (see lower panels in Fig. 11), in spite of the complicated electronic structure of the many bands lying in the valence state, the band structure near E_F is rather simple. For the calculations without SOC [Fig. 11(a)], there exist only two bands crossing E_F. On the $T_X - Z$ and $Z - T_Y$ lines, a twofold-degenerated band crosses the E_F once for each. This band splits into two separate bands on the T_Y-Y line. One of two (lower-energy band) once crosses E_F on the T_Y-Y line, forming a Fermi surface. Another nondegenerated band (higher-energy band) crosses E_F on the Y-Γ line twice, forming a small Fermi surface like an electron pocket between the Y and Γ points. The higher-energy band also crosses E_F on the Γ-Z line, forming another Fermi surface. The SOC alters the degeneracies and dispersions of energy bands as shown in Fig. 11(b), resulting in the significant modification of Fermi surfaces. On the $T_X - Z - T_Y$ lines, the two split bands cross E_F and form two kinds of Fermi surfaces. The splitting due to SOC is around $\Delta_{SO} \sim 0.12$ eV for the bands near E_F. At general k points including the X-Γ-Y, T_Y-Y, and Γ-Z lines, the bands, which are twofold degenerated by spin, further split into two subbands by the antisymmetric part of SOC. The spin-splitting bands cross E_F on the T_Y-Y, Y-Γ, and Γ-Z lines and form spin-splitting Fermi surfaces. The splitting due to antisymmetric SOC is around $\Delta_{ASO} \sim 0.07$ eV for the bands near E_F.

Figure 13 shows the shape of the Fermi surfaces in $BaIrSi_2$. Figures 13(a) and 13(b) show an overview of the Fermi surfaces without and with SOC, respectively. Figure 13(c) depicts k_z-axis cross sections of the Fermi surfaces for superposition of two calculation results without SOC (black broken lines) and with SOC (green and red lines). When SOC is not included, two kinds of Fermi surfaces [colored by green or brown for each in Fig. 13(a)] exist, originating in different bands. One is the large Fermi surface (green curved surface) connecting to the neighboring Brillouin zones, situated around the Γ-Z axis. The other is the Fermi surface (brown curved surface) closed in the first Brillouin zone around the Z point, situated inside the former (green) Fermi surface. These Fermi surfaces merge together at the $k_z = \pm 1/2$ Brillouin-zone boundary, for the degeneracy due to crystallographic symmetry. There is an additional isolated small Fermi surface of an electron pocket (brown closed shell) around the Γ-Y axis, which is derived from the latter (brown inner) Fermi surface. They have the same band origin. On the other hand, an antisymmetric part of SOC splits a Fermi surface into two distinct surfaces at general k points except for the $k_z = \pm 1/2$ Brillouin-zone boundary. Each of the Fermi surfaces is completely divided into a couple of spin-splitting Fermi surfaces by antisymmetric SOC. The small electron pocket also splits into two subparts. One of two (outside surface) is fused with one of the other Fermi surfaces situated around the Z point. In total there are four spin-splitting Fermi surfaces in the Brillouin zone. Most of the electrons are spin splitting on the Fermi surfaces. However, on the $k_z = \pm 1/2$ Brillouin-zone boundary, the degeneration still survives due to crystal symmetry. The energy bands preserve the twofold degeneracy only on the two coaxial closed lines in the $k_z = \pm 1/2$ plane.

The cross sections of the Fermi surfaces exhibit a scale of Fermi-surface splitting in k space. As shown in the cross sections cutting at $k_z = 5/20$–$9/20$ [in Fig. 13(c)], sizable Fermi-surface splitting occurs everywhere on the Fermi surfaces in the k space. The typical distance between two spin-splitting Fermi surfaces in a k_z plane is $\Delta q \sim 0.08\,\mathrm{nm}^{-1}$. In the superconducting state the wave function of Cooper pairs can be affected by the perturbation with a degree of the Δq size. The size of Δq is roughly over one-half of the inverse of the superconducting coherence length, $q_0 = 1/\xi_0 \sim 0.13\,\mathrm{nm}^{-1}$. This suggests that such perturbation against the superconducting wave function is not enough for pair breaking, but it does not seem to be a negligible size for superconductivity. Cooper

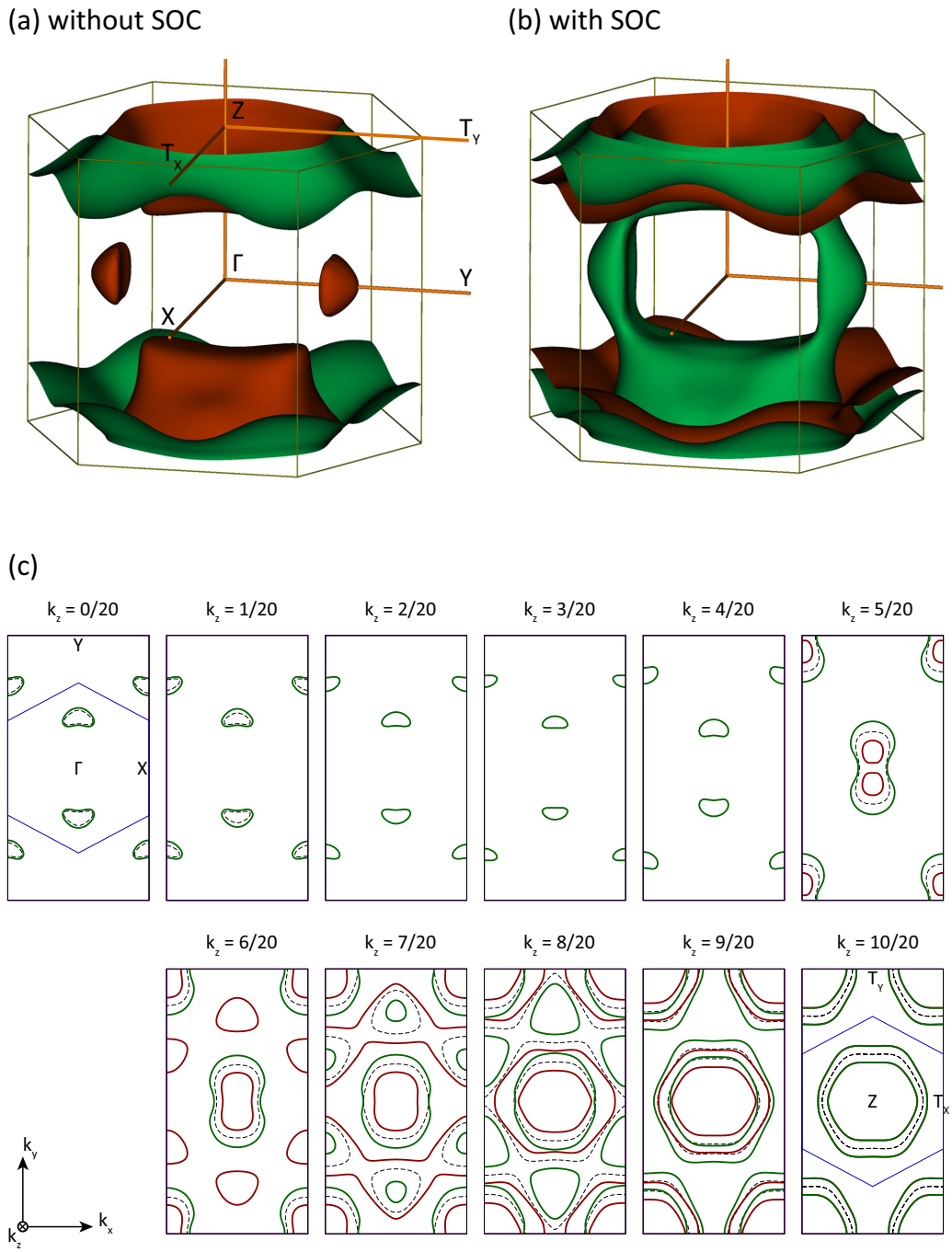

FIG. 13. Fermi surfaces in $BaIrSi_2$. (a, b) Overview of the Fermi surfaces, for the calculations without SOC and with SOC, respectively. (c) Cross sections of the Fermi surfaces, cutting at $k_z = i/20$ ($i = 0$–10). Two calculation results (without SOC and with SOC) are drawn for superposition on a sheet. The black broken lines indicate Fermi surfaces without SOC, while the green and red lines are nondegenerate Fermi surfaces with SOC. The blue line shows the first Brillouin zone (BZ). The labels indicate symmetric points for the orthorhombic base-centered lattice: $\Gamma = (000)$, $X = (100)$, $Y = (010)$, $Z = (001)$, $T_X = (101)$, and $T_Y = (011)$. X,T_X, and Z are on the BZ boundary, while Y and T_Y are located outside of the first BZ.

pairing on the spin-splitting Fermi surfaces may affect the superconducting state in $BaIrSi_2$.

IV. CONCLUSIONS

We successfully synthesized a $5d$ electron system superconductor $BaIrSi_2$ using a high-pressure synthesis technique at 1600 °C under 6 GPa. STEM and x-ray Rietveld analysis studies revealed that $BaIrSi_2$ crystallizes in an orthorhombic structure with the noncentrosymmetric space group $C222_1$ and the lattice parameters $a = 15.0492(1)$ Å, $b = 8.0311(1)$ Å, and $c = 8.0314(1)$ Å. The structure accommodates two kinds of Si polyhedrons surrounding Ir atoms. The Ir-Si_4 tetrahedron and the Ir-Si_6 octahedron are distorted,

forming an asymmetric crystal field around the Ir atoms, presumably giving rise to antisymmetric spin-orbit coupling in $BaIrSi_2$.

$BaIrSi_2$ shows type-II bulk superconductivity below a critical temperature $T_c \sim 6\,\mathrm{K}$, an upper critical field $\mu_0 H_{c2}(0) \sim 6\,\mathrm{T}$, and a Ginzburg-Landau parameter $\kappa_{\mathrm{GL}} \sim 87$. The normal range of the Sommerfeld constant $\gamma_n \sim 5.5\,\mathrm{mJ/mole\,K^2}$ suggests a conventional Fermi-liquid behavior with a small effective-mass enhancement for electron correlation. Phonon mediation seems to be dominant for Cooper pairing in $BaIrSi_2$. The behavior in T-dependent electronic specific heat $C_{\mathrm{el}}'(T)$ suggests a full-gap (nodeless-gap) character with possible dominant spin-singlet s-wave Cooper pairing in $BaIrSi_2$. The specific-heat jump $\Delta C_{\mathrm{el}}/(\gamma_n T_c) \sim 1.65$ at the superconducting transition suggests intermediate-coupling superconductivity with a moderate electron-phonon interaction of $\lambda_{ep} \sim 0.8$. Other superconducting parameters are summarized in Table II.

Ab initio calculation revealed that in $BaIrSi_2$ the valence state near E_F mainly consists of the Ir-5d and Si-3p hybridized bands, and that SOC splits degeneracy of the twofold bands and shifts the bands in energy. At general k points in the Brillouin zone, the electronic band splits into two subbands due to the antisymmetric part of SOC for the noncentrosymmetric crystal structure. The band-splitting energy size is around $\Delta_{\mathrm{ASO}} \sim 0.07\,\mathrm{eV}$ near E_F. Under SOC, there are four Fermi surfaces in the Brillouin zone, as shown in Fig. 13(b). Most of the bands, except for the minority on the $k_z = \pm 1/2$ zone boundary, are spin splitting on the Fermi surfaces. The Cooper pairing seems to occur mostly on the spin-splitting Fermi surfaces. The typical size of the Fermi-surface splitting in k space is $\Delta q \sim 0.08\,\mathrm{nm^{-1}}$, which is just over one-half of the inverse of the superconducting coherence length, $q_0 = 1/\xi_0 \sim 0.13\,\mathrm{nm^{-1}}$. In the superconducting state, the wave function of Cooper pairs could be affected by the perturbation with a degree of the Δq size in $BaIrSi_2$.

ACKNOWLEDGMENTS

We sincerely thank Dr. T. Taniguchi of National Institute for Materials Science (NIMS) for technical support on high-pressure synthesis experiments, Mr. M. Nishio of NIMS for EPMA measurements, and Dr. Y. Matsui of NIMS for fruitful discussion about the crystal symmetry. M.I. thanks Ms. E. Hashimoto of NIMS for assistance in experiments. This work was carried out within the Research Project administrated by NIMS, and partly supported by Japan Society for the Promotion of Science through Grants-in-Aid for Scientific Research (Grant No. 16K06712). Part of the calculations in this study were performed on the Numerical Materials Simulator at NIMS.

[1] G. Jackeli and G. Khaliullin, Phys. Rev. Lett. **102**, 017205 (2009).
[2] H. Watanabe, T. Shirakawa, and S. Yunoki, Phys. Rev. Lett. **105**, 216410 (2010); **110**, 027002 (2013).
[3] J. Kim, M. Daghofer, A. H. Said, T. Gog, J. van den Brink, G. Khaliullin, and B. J. Kim, Nat. Commun. **5**, 4453 (2014), and references therein.
[4] *Non-Centrosymmetric Superconductors, Introduction and Overview*, Lecture Notes in Physics Vol. 847, edited by E. Bauer and M. Sigrist (Springer-Verlag, Berlin, 2012).
[5] E. Bauer, H. Kaldarar, A. Prokofiev, E. Royanian, A. Amato, J. Sereni, W. Brämer-Escamilla, and I. Bonalde, J. Phys. Soc. Jpn. **76**, 051009 (2007).
[6] V. M. Edelstein, Sov. Phys. JETP **68**, 1244 (1989); Phys. Rev. Lett. **75**, 2004 (1995).
[7] L. P. Gor'kov and E. I. Rashba, Phys. Rev. Lett. **87**, 037004 (2001).
[8] P. A. Frigeri, D. F. Agterberg, A. Koga, and M. Sigrist, Phys. Rev. Lett. **92**, 097001 (2004).
[9] S. Fujimoto, J. Phys. Soc. Jpn. **76**, 051008 (2007); **76**, 034712 (2007); **75**, 083704 (2006); Phys. Rev. B **72**, 024515 (2005); Butsuri **63**, 18 (2008).
[10] N. Hayashi, K. Wakabayashi, P. A. Frigeri, and M. Sigrist, Phys. Rev. B **73**, 024504 (2006); **73**, 092508 (2006); N. Hayashi and M. Sigrist, Kotai Butsuri **41**, 631 (2006).
[11] Y. Yanase and M. Sigrist, J. Phys. Soc. Jpn. **76**, 124709 (2007).
[12] E. Bauer, G. Hilscher, H. Michor, Ch. Paul, E. W. Scheidt, A. Gribanov, Yu. Seropegin, H. Noël, M. Sigrist, and P. Rogl, Phys. Rev. Lett. **92**, 027003 (2004).
[13] N. Kimura, K. Ito, K. Saitoh, Y. Umeda, H. Aoki, and T. Terashima, Phys. Rev. Lett. **95**, 247004 (2005).
[14] I. Sugitani, Y. Okuda, H. Shishido, T. Yamada, A. Thamizhavel, E. Yamamoto, T. D. Matsuda, Y. Haga, T. Takeuchi, R. Settai, and Y. Ōnuki, J. Phys. Soc. Jpn. **75**, 043703 (2006).
[15] R. Settai, I. Sugitani, Y. Okuda, A. Thamizhavel, M. Nakashima, Y. Ōnuki, and H. Harima, J. Magn. Magn. Mater. **310**, 844 (2007).
[16] T. Akazawa, H. Hidaka, H. Kotegawa, T. C. Kobayashi, T. Fujiwara, E. Yamamoto, Y. Haga, R. Settai, and Y. Ōnuki, J. Phys. Soc. Jpn. **73**, 3129 (2004).
[17] E. Bauer, R. T. Khan, H. Michor, E. Royanian, A. Grytsiv, N. Melnychenko-Koblyuk, P. Rogl, D. Reith, R. Podloucky, E.-W. Scheidt, W. Wolf, and M. Marsman, Phys. Rev. B **80**, 064504 (2009).
[18] G. Eguchi, D. C. Peets, M. Kriener, Y. Maeno, E. Nishibori, Y. Kumazawa, K. Banno, S. Maki, and H. Sawa, Phys. Rev. B **83**, 024512 (2011).
[19] M. Isobe, M. Arai, and N. Shirakawa, Phys. Rev. B **93**, 054519 (2016).
[20] K. Togano, P. Badica, Y. Nakamori, S. Orimo, H. Takeya, and K. Hirata, Phys. Rev. Lett. **93**, 247004 (2004).
[21] P. Badica, T. Kondo, and K. Togano, J. Phys. Soc. Jpn. **74**, 1014 (2005).
[22] B. T. Matthias, V. B. Compton, and E. Corenzwit, J. Phys. Chem. Solids **19**, 130 (1961).
[23] T. Klimczuk, Q. Xu, E. Morosan, J. D. Thompson, H. W. Zandbergen, and R. J. Cava, Phys. Rev. B **74**, 220502 (2006).

[24] J. Johnston, L. E. Toth, K. Kennedy, and E. R. Parker, Solid State Commun. **2**, 123 (1964).
[25] W. H. Lee, H. K. Zeng, Y. D. Yao, and Y. Y. Chen, Physica C **266**, 138 (1996).
[26] M. C. Krupka, A. L. Giorgi, N. H. Krikorian, and E. G. Szklarz, J. Less-Common Met. **17**, 91 (1969).
[27] G. Amano, S. Akutagawa, T. Muranak, Y. Zenitani, and J. Akimitsu, J. Phys. Soc. Jpn. **73**, 530 (2004).
[28] A. Simon and T. Gulden, Z. Anorg. Allg. Chem. **630**, 2191 (2004).
[29] B. T. Matthias, T. H. Geballe, and V. B. Compton, Rev. Mod. Phys. **35**, 1 (1963).
[30] R. D. Blaugher and J. K. Hulm, J. Phys. Chem. Solids **19**, 134 (1961).
[31] T. Shibayama, M. Nohara, H. Aruga-Katori, Y. Okamoto, Z. Hiroi, and H. Takagi, J. Phys. Soc. Jpn. **76**, 073708 (2007).
[32] E. Bauer, H. Kaldarar, R. Lackner, H. Michor, W. Steiner, E.-W. Scheidt, A. Galatanu, F. Marabelli, T. Wazumi, K. Kumagai, and M. Feuerbacher, Phys. Rev. B **76**, 014528 (2007).
[33] M. Hanawa, Y. Muraoka, T. Tayama, T. Sakakibara, J. Yamaura, and Z. Hiroi, Phys. Rev. Lett. **87**, 187001 (2001).
[34] M. Nishiyama, Y. Inada, and Guo-qing Zheng, Phys. Rev. Lett. **98**, 047002 (2007).
[35] A. D. Hillier, J. Quintanilla, and R. Cywinski, Phys. Rev. Lett. **102**, 117007 (2009).
[36] K. Kimoto, T. Asaka, X. Yu, T. Nagai, Y. Matsui, and K. Ishizuka, Ultramicroscopy **110**, 778 (2010).
[37] F. Izumi and K. Momma, Solid State Phenom. **130**, 15 (2007).
[38] P. Blaha, K. Schwarz, G. K. H. Madsen, D. Kvasnicka, J. Luitz, R. Laskowski, F. Tran, and L. D. Marks, *WIEN2K: An Augmented Plane Wave Plus Local Orbitals Program for Calculating Crystal Properties* (Karlheinz Schwarz, Technische Universität Wien, Wien, Austria, 2001).
[39] J. P. Perdew, K. Burke, and M. Ernzerhof, Phys. Rev. Lett. **77**, 3865 (1996).
[40] P. Hohenberg and W. Kohn, Phys. Rev. **136**, B864 (1964).
[41] S. D. Findlay, N. Shibata, H. Sawada, E. Okunishi, Y. Kondo, and Y. Ikuhara, Ultramicroscopy **110**, 903 (2010).
[42] The magnetic susceptibility data are as-measured values without any correction. The signal intensity $4\pi\chi$ indicates a rough estimate of the superconducting volume fraction. It, strictly speaking, may be a little different from the accurate volume of the superconducting phase in the sample, owing to demagnetization effect and magnetic-flux penetration in the superconducting phase.
[43] W. L. McMillan, Phys. Rev. **167**, 331 (1968).
[44] P. B. Allen and R. C. Dynes, Phys. Rev. B **12**, 905 (1975).
[45] F. Marsiglio and J. P. Carbotte, Phys. Rev. B **33**, 6141 (1986).
[46] J. P. Carbotte, Rev. Mod. Phys. **62**, 1027 (1990).
[47] P. Morel and P. W. Anderson, Phys. Rev. **125**, 1263 (1962).
[48] K. Miyake, Kotai Butsuri **31**, 745 (1996).
[49] B. Mühlschlegel, Z. Phys. **155**, 313 (1959).
[50] In Fig. 10, the different T dependence between T_c^{bulk} and T_c^{onset} data lines seems to be a rather typical, frequently observed feature of noncentrosymmetric superconductors (see, e.g., [18]).
[51] K. Maki and T. Tsuneto, Prog. Theor. Phys. **31**, 945 (1964).
[52] R. R. Hake, Appl. Phys. Lett. **10**, 189 (1967).
[53] A. M. Clogston, Phys. Rev. Lett. **9**, 266 (1962).
[54] E. Helfand and N. R. Werthamer, Phys. Rev. **147**, 288 (1966).
[55] N. R. Werthamer, E. Helfand, and P. C. Hohenberg, Phys. Rev. **147**, 295 (1966).
[56] L. N. Bulaevskii, O. V. Dolgov, and M. O. Ptitsyn, Phys. Rev. B **38**, 11290 (1988).
[57] P. C. Hohenberg and N. R. Werthamer, Phys. Rev. **153**, 493 (1967).
[58] V. G. Kogan and R. Prozorov, Phys. Rev. B **88**, 024503 (2013).